Pergamon

Int. J. Heat Mass Transfer. Vol. 40, No. 6, pp. 1325–1341, 1997

0017–9310/97 $17.00+0.00

PII: S0017–9310(96)00207–4

Computations of flow and heat transfer in parallel-plate fin heat exchangers on the CM-5: effects of flow unsteadiness and three-dimensionality

L. W. ZHANG,† D. K. TAFTI,‡§ F. M. NAJJAR‡ and S. BALACHANDAR¶

†Department of Mechanical and Industrial Engineering, ‡National Center for Supercomputing Applications, ¶Department of Theoretical and Applied Mechanics, University of Illinois at Urbana-Champaign, Urbana, IL 61801, U.S.A.

(*Received* 13 *February* 1996 *and in final form* 29 *May* 1996)

Abstract—An accurate computational method for the calculation of flow and heat transfer in compact heat exchangers is developed and implemented on the massively parallel Connection Machine, CM-5. In this method, the unsteady Navier–Stokes and energy equations are solved. The current study shows that the inclusion of flow unsteadiness plays a very important role in the accurate prediction of heat exchanger performance quantities of interest such as the Colburn *j* factor and the friction factor. It is also shown that at higher Reynolds numbers, the additional effect introduced by the intrinsic three-dimensionality of the flow plays another important role in determining the overall heat exchanger performance. Therefore, the above two effects have to be taken into account in order to accurately predict heat exchanger performance.

INTRODUCTION

Understanding the heat transfer enhancement mechanisms associated with interrupted surfaces in compact heat exchangers is an important area of research [1–3]. Surface interruptions are commonly used for heat transfer enhancement. These not only increase the heat transfer surface area per unit volume, but also modify the fluid dynamics to augment the heat transfer coefficient. At the same time the interrupted surfaces also increase the pressure drop and subsequently the pumping power. From the fluid dynamics viewpoint, the flow in these fin arrays provides a rich kaleidoscope of flow phenomena. Depending on the Reynolds number and the fin geometry, flow within these fin arrays could be laminar, with or without flow separation, transitional, or finally, turbulent [4].

Computational modeling of these flows has been used in the past and is becoming increasingly popular. Most previous numerical studies have made critical assumptions in the solution of the Navier–Stokes and energy equations; namely the flow and thermal fields are assumed to be steady and two-dimensional. For example, Sparrow and Liu [5] have studied heat transfer on a series of parallel infinitesimally thin flat plates placed in inline and staggered arrangements. By using an approximate parabolic form of the steady Navier–Stokes and energy equations, they included the entrance and exit effects. Patankar and Prakash [6] solved the Navier–Stokes and energy equations under steady state assumption, to study the heat transfer from a series of finite thickness plates in a staggered arrangement. This and their earlier study (Patankar *et al.* [7]) have provided an analytical/computational frame work within which the thermal behavior of a large array of fins can be modeled by assuming the flow to be periodic along the streamwise direction.

The assumption of steady flow and thermal fields precludes much of the flow physics, particularly in situations when the flow is dominated by large scale time-dependent variations. Recent simulations of flows in grooved and communicating channels by Ghaddar *et al.* [8], Amon and Mikic [9] have included time-dependence in their simulations. However the effect of unsteadiness has not been fully isolated and quantified. Furthermore, even in the case of nominally two-dimensional fins at sufficiently high Reynolds numbers, due to intrinsic instabilities, the flow becomes three-dimensional and the effect of three-dimensionality on heat transfer and pressure drop can be significant (Mittal and Balchandar [10], Tafti and Vanka [11]).

The purpose of the present study is to isolate and quantify the importance of incorporating the effects of time-dependence and three-dimensionality on the prediction of heat transfer and pressure drop in a large array of fins. Here we have performed simultaneous time-dependent and steady-state calculations under otherwise identical conditions, and the difference between the two calculations highlights the import-

---

§Author to whom correspondence should be addressed.

NOMENCLATURE

b	fin thickness
C	transverse adjacent fin spacing, Fig. 1
C_p	specific heat of the fluid
D_h	hydraulic diameter
$\mathbf{e}_x$	unit vector in streamwise, x, direction
f	friction factor
F	primary shedding frequency
H	half channel height, Fig. 1
j	modified Colburn factor
k	thermal conductivity of the fluid
L	fin length
L_x	computational domain length in x-direction, Fig. 1
L_y	computational domain length in y-direction, Fig. 1
m	number of rows of fins in y-direction
n	number of columns of fins in x-direction
$\mathbf{n}$	outward normal unit vector on fin surface
Nu	Nusselt number
$\langle Nu \rangle$	global Nusselt number
ΔP	mean pressure difference along flow direction
P	total pressure
p	modified perturbation pressure
Pr	Prandtl number
Q	mean flow rate per unit spanwise width
q''	constant heat flux
Re	Reynolds number
S	streamwise adjacent fin spacing, Fig. 1
Str	Strouhal number
t	time
T	total temperature
u, v, w	velocity in x-, y- and z-directions
u_τ	friction velocity
V	mean flow velocity at minimum flow cross-section area
W	spanwise width of the fin.

Greek symbols

β	mean pressure gradient
δ_{ij}	Kronecker delta
γ	mean temperature gradient
θ	modified perturbation temperature
ρ	density of the fluid
Ω_f	fin surface area.

Superscript

$*$	dimensional quantities.

Subscripts

b	based on fin thickness
f	based on the fin
i,j	based on x, y, z Cartesian coordinates
in	quantity at the inlet of computational domain
ref	reference quantity
x, y	based on x, y Cartesian coordinates
τ	based on friction velocity.

ance of unsteady flow phenomena. Corresponding 3-D simulations at high Reynolds numbers have also been performed to identify the effect of three-dimensionality. These effects have been investigated over a range of Reynolds numbers which are well within typical compact heat exchanger operating conditions. A finite-volume based numerical algorithm has been developed to solve the incompressible Navier–Stokes and energy equations in two- or three-dimensions in a time-accurate manner. A computer program based on this methodology has been implemented on the massively parallel CM-5 in the single instruction multiple data (SIMD) or the data parallel programing paradigm.

In the following sections, the mathematical formulation and the numerical methodology will be described. Then the parallel performance on the CM-5 will be shown, along with some grid dependency study results. Finally, the effects of flow unsteadiness and three-dimensionality on flow and heat transfer will be quantified.

GOVERNING EQUATIONS AND SOLUTION ALGORITHM

For computational purposes, a large array of fins can be approximated by a simpler system, made up of periodic repetition of a basic unit and the computational domain can be limited to this basic unit [6–9]. Implicit in this treatment is the assumption that the flow is fully developed, both hydrodynamically and thermally, in the fin array and excluding any entrance or exit effects. However, this does not detract considerably from the real situation where most of the heat transfer would occur in the fully developed flow regime [7]. Figure 1 shows nine fin elements arranged in inline fashion within a heat exchanger consisting of a large array of these fins. The computational domain is indicated by the dashed line, consisting of only one fin element with appropriate periodic boundary conditions imposed along both the streamwise (x) and transverse (y) directions. The computational domain, along with the appropriate periodic boundary con-

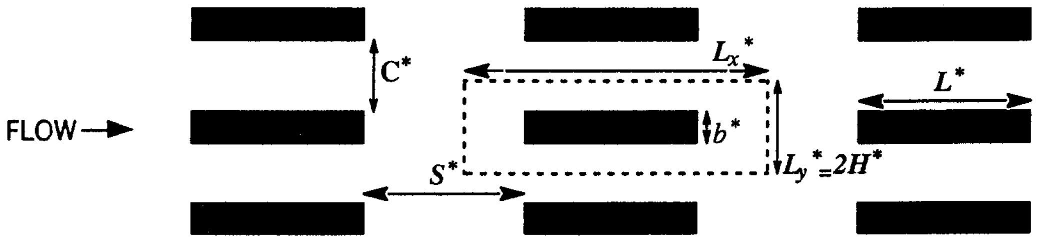

Fig. 1. A schematic of the geometry simulated and the computational domain.

ditions, will serve as a model for the large arrays of fins.

The time-dependent, incompressible continuity, momentum, and energy equations are of the following *nondimensional* form:

$$\frac{\partial u_i}{\partial x_i} = 0 \tag{1}$$

$$\frac{\partial u_i}{\partial t} + \frac{\partial}{\partial x_j}(u_i u_j) = -\frac{\partial P}{\partial x_i} + \frac{1}{Re_\tau}\frac{\partial^2 u_i}{\partial x_j^2} \tag{2}$$

$$\frac{\partial T}{\partial t} + \frac{\partial}{\partial x_j}(u_i T) = \frac{1}{Re_\tau Pr}\frac{\partial^2 T}{\partial x_j^2} \tag{3}$$

where $i = 1, 2, 3$ corresponds to $x(u)$, $y(v)$, and $z(w)$ coordinates (velocities) in three dimensions, respectively. Equations (1)–(3) are nondimensionalized by using: half width of the computational domain ($H^* = (b^* + C^*)/2$) as the length scale, the friction velocity ($u_\tau^* = \sqrt{\Delta P^*/\rho}$) as the velocity scale, ΔP^* as the pressure scale, H^*/u_τ^* as the time scale and $q''^* H^*/k$ as the temperature scale, where ΔP^* is the applied dimensional pressure drop over a streamwise length of H^*, q''^* is the specified dimensional constant heat flux along the fin surface and k is the thermal conductivity of the fluid. The above nondimensionalization results in two dimensionless parameters in the above governing equations: the Reynolds number based on friction velocity $Re_\tau = u_\tau^* H^*/\nu$ and the Prandtl number $Pr = \nu/\alpha$, where ν and α are the kinematic viscosity and thermal diffusivity of the fluid, respectively. Furthermore, in the remainder of the paper we will mainly consider only nondimensional quantities. Any use of dimensional quantities will be explicitly stated and denoted by superscript * except that of constant material properties.

While the periodic nature of the geometry along both the x and y directions is evident from the fin arrangement considered in Fig. 1, the imposition of periodic boundary conditions in the streamwise direction on the flow variables pressure and temperature, is not straight forward. In fact, pressure decreases along the flow direction and fluid temperature either increases or decreases along the flow direction depending on heat transfer between the fluid and the fin surface. It has been shown in the past by Patankar and co-workers [6, 7] that by subtracting these mean variations along the flow direction, modified pressure and modified temperature variables can be defined, which admit a periodic solution along the streamwise direction. This necessitates reformulation of the governing equations (1)–(3) in terms of the modified variables. This approach has been adopted by a number of later investigations, including the more recent efforts by Ghaddar *et al.* [8], Amon and Mikic [9].

The nondimensional total pressure P will be separated into a linear component and a modified nondimensional pressure p as follows:

$$P(x, y, t) = P_{\text{in}} - \beta x + p(x, y, t) \tag{4}$$

where, P_{in} is the arbitrary nondimensional pressure at the inlet of the computational domain, and β is the linear component of the nondimensional pressure gradient in the flow direction. Therefore by choosing β to be a constant (in this case unity), the linear pressure variation can be made to completely account for the mean pressure drop across the computational domain and the modified pressure p can then be assumed to be periodic along the streamwise direction. Thus the resulting mean pressure difference across the computational domain balances the frictional losses within the computational domain. Therefore in the present computations the streamwise pressure gradient is held fixed and the computed flow rate adjusts over time, in order for the frictional losses to instantaneously balance the applied pressure force. It must be pointed out that the linear pressure variation accurately accounts for the mean pressure variation only across the entire streamwise periodic boundaries. The actual mean nondimensional pressure variation along the streamwise direction will depart significantly from the linear variation and therefore the mean streamwise gradient of the modified nondimensional pressure, defined as $\partial/\partial x[1/2\int_{-1}^{1} p(x, y, t)\,\mathrm{d}y]$, will in general be nonzero. But the mean modified nondimensional pressure difference across the computational domain, $\int_0^{L_x} \partial/\partial x[1/2\int_{-1}^{1} p(x, y, t)\,\mathrm{d}y]\,\mathrm{d}x$, will be identically zero.

Based on the above arguments periodic boundary conditions of the following general form can be applied for both the nondimensional velocity and modified nondimensional pressure fields as:

$$u_i(x + nL_x, y + mL_y) = u_i(x, y) \tag{5}$$

$$p(x + nL_x, y + mL_y) = p(x, y). \tag{6}$$

In the above it is assumed that the computational domain consists of m rows of fins in the y-direction and n columns of fins in the x-direction. Such general periodic boundary conditions as a model for flow over a periodically repeating geometry have been considered in the past by other investigators [6–9]. Here results will be presented for the case of $m = 1$ and $n = 1$. On the fin surfaces, no slip and no penetration boundary conditions are applied for the velocities while Neumann boundary condition of the following type is applied for the modified nondimensional pressure ([12, 13]):

$$\nabla p \cdot \mathbf{n} = 0 \tag{7}$$

where $\mathbf{n}$ is the unit vector along the outward normal to the fin surface.

Similarly the nondimensional temperature field, T, can be decomposed into a linear part and a modified nondimensional temperature, θ, as

$$T(x, y, t) = T_{\text{in}} + \gamma x + \theta(x, y, t) \tag{8}$$

where T_{in} is the arbitrary nondimensional inlet temperature, γx specifies the linear portion of the nondimensional temperature variation along the streamwise direction due to the constant heat flux boundary condition on the fin surface. Performing a global energy balance dictates a dimensional mean temperature change of $q''^{*}\Omega_{\text{f}}^{*}/\rho C_{\text{p}}(Q^{*}W^{*})$ from the inlet to the outlet of the domain, where $\Omega_{\text{f}}^{*} = 2W^{*}(L_{x}^{*}+b^{*})$ is the fin surface area, C_{p} is the specific heat of the fluid, W^{*} is the spanwise width of the fin, and Q^{*} is the flow rate per unit width along the z-direction. Hence, the nondimensional temperature gradient γ can be written in terms of the corresponding nondimensional variables as

$$\gamma = \frac{2(L+b)}{Re_{\tau}PrQL_{x}}. \tag{9}$$

By substituting the nondimensional temperature decomposition, equation (8), into the energy equation, equation (3), and ignoring any time dependence of γ, we obtain an equation for the modified nondimensional temperature as

$$\frac{\partial \theta}{\partial t} + u\gamma + \frac{\partial}{\partial x_{j}}(u_{j}\theta) = \frac{1}{Re_{\tau}Pr}\frac{\partial^{2}\theta}{\partial x_{j}^{2}} \tag{10}$$

where the modified nondimensional temperature θ can also be considered to be periodic along both the streamwise and transverse directions and satisfies the following general condition [6–9]:

$$\theta(x+nL_{x}, y+mL_{y}) = \theta(x, y). \tag{11}$$

Furthermore from equation (8), the constant dimensional heat flux at the fin surface reduces to the following boundary condition for the modified nondimensional temperature at the fin surface

$$\nabla\theta \cdot \mathbf{n} = 1 - \gamma \mathbf{e}_{x} \cdot \mathbf{n} \tag{12}$$

where $\mathbf{e}_{x}$ is the unit vector along the x-direction.

From the above discussion it is clear that the definition of modified nondimensional temperature according to equation (8) and the subsequent periodic boundary condition in the streamwise direction on computational domain boundaries are made possible by the constant heat flux boundary condition, which provides a precise measure of the temperature difference between the inlet and outlet of the computational domain. With isothermal boundary condition, since the fluid temperature continuously either increases or decreases downstream depending on the direction of heat transfer between the fin surface and the fluid, application of periodic thermal boundary condition along the streamwise direction is not straight forward. Modified temperature and appropriate periodic boundary condition based on a self similar development of the thermal profiles have been proposed by Patankar *et al.* [7] in the steady flow regime. To our knowledge formulation of this problem in the unsteady flow regime has not been performed.

The above modified Navier–Stokes and energy equations are solved on a staggered grid in which the velocity nodes are staggered halfway between the scalar nodes in their respective coordinate directions. The resulting equations are discretized by using finite-volume approximations for the convection and viscous terms, which utilize second-order central differences [14].

Time integration of the discretized momentum equations is performed by using the fractional-step method (Chorin [15] and also Kim and Moin [16]). In brief, first an intermediate velocity field ($\tilde{u}_{i}$) is calculated by neglecting the contribution of the pressure gradient term to momentum balance. The time advancement of this step is performed by using an explicit second-order accurate Adams–Bashforth approximation. Next the intermediate velocity field is made divergence free (u_{i}^{n+1}) by solving a pressure Poisson equation for pressure, p^{n+1}. These steps can be represented by the following equations:

$$\frac{\tilde{u}_{i} - u_{i}^{n}}{\Delta t} = \delta_{i1} + \frac{3}{2}H_{i}^{n} - \frac{1}{2}H_{i}^{n-1} \tag{13}$$

and

$$H_{i} = -\frac{\partial}{\partial x_{j}}(u_{i}u_{j}) + \frac{1}{Re_{\tau}}\frac{\partial^{2}u_{i}}{\partial x_{j}^{2}}. \tag{14}$$

The correction to make the velocity field divergence free and include the effects of the pressure gradient is given by:

$$u_{i}^{n+1} = \tilde{u}_{i} - \Delta t\frac{\partial p^{n+1}}{\partial x_{i}}. \tag{15}$$

The pressure field p^{n+1} is obtained by applying the continuity equation at time $(n+1)$ to equation (15) and solving the resulting pressure Poisson equation:

$$\frac{\partial}{\partial x_{i}}\left\{\frac{\partial p^{n+1}}{\partial x_{i}}\right\} = \frac{1}{\Delta t}\frac{\partial \tilde{u}_{i}}{\partial x_{i}}. \tag{16}$$

The energy equation is advanced in time by using a fully explicit second-order Adams–Bashforth approximation as follows:

$$\frac{\theta^{n+1}-\theta^{n}}{\Delta t}=\frac{3}{2}\Lambda^{n}-\frac{1}{2}\Lambda^{n-1} \tag{17}$$

where Λ is given by:

$$\Lambda=-\gamma u-\frac{\partial}{\partial x_j}(u_j\theta)+\frac{1}{Re_\tau Pr}\frac{\partial^2\theta}{\partial x_j^2}. \tag{18}$$

In a typical flow simulation, the hydrodynamic flow field is allowed to reach a fully developed state before the heat transfer calculations are initiated. Once the flow rate has reached a fully developed state,† the heat transfer calculations are initiated with an initial field of $\theta = 0$. Subsequently the time evolution of the average Nusselt number at the fin surface is monitored to determine the fully developed thermal state.

In the three-dimensional computations the spanwise direction is considered to be periodic and periodic boundary conditions were applied for the velocity, pressure and temperature fields along the z-direction. The present computations to be reported were performed with a nondimensional spanwise extent of $4b$. At Reynolds numbers just above the critical value for the onset of three-dimensionality, as considered here, it has been observed that the wake behind bluff bodies (Wu *et al.* [17], Mansy *et al.* [18], Henderson [19], Williamson [20]) exhibits three-dimensionality in the form of periodic structures with spanwise wave lengths ranging from 0.8 to 4 times the height of the bluff body. But no such results exist for flow around a periodic array of flat plates of finite thickness and based on the bluff body results a spanwise extent of $4b$ is chosen to capture the essential 3-D physics and topological features of the flow, with adequate resolution along the spanwise direction. Although a bigger computation domain along the spanwise direction may be desirable the corresponding well resolved simulations can be prohibitively expensive.

RESULTS AND DISCUSSION

1. *Parallel performance*

The discretized governing equations are solved on the Connection Machine-5 (CM-5). The CM-5 at the National Center for Supercomputing Applications (NCSA) is a massively parallel computer architecture containing 512 processing nodes (each processor has four vector units) with 32 MBytes of memory for each node and a collective memory of 16 GBytes. The work described in this paper was developed based on a general purpose computer program on the CM-5 in the data parallel paradigm [21] for the direct and large eddy simulations of turbulence. The computer program has several features ranging from: second-order to high-order accurate finite-difference approximations, explicit/semi-implicit time advancement algorithms, the ability to handle a mix of boundary conditions, with different solution techniques for the pressure equation. These features, benchmark solutions and validations of the flow solvers, can be found in Tafti refs. [22, 23].

For flows with two homogeneous directions (e.g. turbulent channel flow calculations) the pressure equation is solved with 2-D FFTs in the homogeneous directions with a direct line solver in the inhomogeneous direction. Using this approach with a semi-implicit treatment of the momentum equations, execution speeds of upto 8.8 GFLOPS s^{-1} have been obtained on 512 processing nodes with 24 million nodes in the calculation domain [22]. In the present study, the flow is inhomogeneous in both directions, and we use the method of conjugate gradients (CG [24]) to solve the pressure equation. The parallel implementation and performance of preconditioned CG and other Krylov subspace based methods can be found in Tafti [25]. In this paper we will show the execution speeds for the grid sizes used in the present study and also the scalability of the computer program for large grid sizes, which would arise in large two- and three-dimensional calculations.

Figure 2 shows the parallel performance of the computer program. The typical performance for the two-dimensional grids used in the current work on a 32-node partition of the CM-5 is plotted in Fig. 2(a). The MFLOP rates are obtained by estimating the floating point operations per second in each module of the computer program. Typically, 97% of the computational time is spent in solving the pressure equation, while the other 3% is spent in the momentum and energy equations. We find that the performance is a modest 100 MFLOPS at a resolution of 128 × 32, but increases rapidly to 450 MFLOPS as the grid resolution increases to 512 × 256. This is a result of increased vector lengths as the problem size increases and the resulting lower communication costs per floating point operation. Furthermore, Fig. 2(b) shows the scalability of the computer program. As the grid size is varied from 512 × 256 on a 32-node partition to 1024 × 1024 on a 256-node partition, a nearly perfect scalability is observed. Extrapolating this result to a 2048 × 1024 grid on a 512-node CM-5 partition gives a performance of 7.0 GFLOPS per second, which clearly indicates the capability of the computer program to solve large scale heat transfer problems.

A typical unsteady simulation with a grid size of 128 × 32 cells requires about 0.3–0.4 second per time

---

† The definition of a fully developed state depends on the flow regime. For flows at low Reynolds numbers, which do not exhibit any vortex shedding, the fully developed state will be characterized by a flow rate (Q) which is truly time independent. In flow regimes with vortex shedding, the flow rate oscillates in time and will exhibit constancy only when averaged suitably. It was found that even at high Reynolds numbers considered here, the instantaneous Q varied less than 0.2% from its mean value, and correspondingly, from equation (9), the neglected time variation in nondimensional temperature gradient, γ, is also very small.

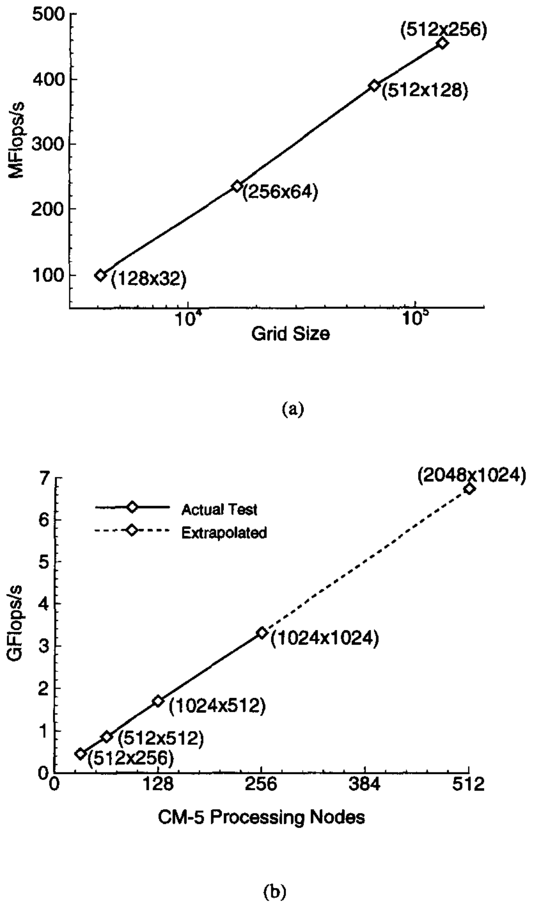

(a)

(b)

Fig. 2. Parallel performance of the program: (a) performance on a 32-node CM-5 partition; (b) scaled performance on CM-5 processing nodes.

step on a 32-node CM-5 partition, depending on the Reynolds number. A typical computation in the time-dependent flow regime requires about 0.8–1.4 nondimensional time units for a shedding cycle. The typical nondimensional time step used in the present computations is of the order of 2×10^{-3}, corresponding to a CFL number of 0.3–0.5. Thus about 2–5 minutes on a 32-node CM-5 partition are needed for a shedding cycle. The simulations are usually performed for more than 50 shedding cycles to ensure a stationary state be reached.

2. *Flow and heat transfer results*

For the presentation of the heat transfer and pressure drop results we define a Reynolds number based on the mean velocity and hydraulic diameter as $Re = V^* D_h^*/\nu$, where V^* is the dimensional mean velocity at the minimum flow cross-sectional area given by (Q^*/C^*) and D_h^* is the dimensional hydraulic diameter defined as $D_h^* = 4C^*W^*/\Omega_f^*/L_x^*$ (see Joshi and Webb ref. [2]). Also presented are the Reynolds number based on the mean velocity and fin thickness as $Re_b = V^*b^*/\nu$. Both these Reynolds numbers can be expressed in terms of Re_τ as $Re = QD_hRe_\tau/C$ and $Re_b = QbRe_\tau/C$, where Q, D_h, b and C are nondimensional flow rate per unit spanwise width, hydraulic diameter, fin thickness and transverse fin spacing, respectively.

We also define a local instantaneous Nusselt number over the fin surface based on the hydraulic diameter as

$$Nu = \frac{D_h^* q''^*/(T_f^* - T_{ref}^*)}{k} \tag{19}$$

where T_f^* and T_{ref}^* are the dimensional fin surface temperature and local reference temperature. In terms of nondimensional quantities the above can be re-written as

$$Nu = \frac{D_h}{\theta_f - \theta_{ref}} \tag{20}$$

where θ_f is the local modified nondimensional fin surface temperature and θ_{ref} is a reference modified nondimensional temperature, which is defined as [6]:

$$\theta_{ref} = \frac{\iint \theta \, |u| \, dy \, dz}{\iint |u| \, dy \, dz}. \tag{21}$$

Based on the local instantaneous Nusselt number we then calculate the instantaneous global Nusselt number integrated over the fin surface as:

$$\langle Nu \rangle = \frac{\Omega_f D_h}{\displaystyle\iint_{\Omega_f} (\theta_f - \theta_{ref}) \, dS}. \tag{22}$$

The mean Nusselt number is then calculated by time averaging $\langle Nu \rangle$ in the fully developed regime and is denoted by $\overline{\langle Nu \rangle}$. Further, we also define the modified Colburn j factor as the measure of heat transfer [26]:

$$j = \frac{\overline{\langle Nu \rangle}}{Re Pr^{0.4}} \tag{23}$$

and a friction factor f as the measure of pressure drop:

$$f = \frac{\Delta P_x^*}{\frac{1}{2}\rho V^{*2}} \left(\frac{D_h^*}{4L_x^*} \right) \tag{24}$$

where ΔP_x^* is the applied streamwise pressure drop across the computational domain. The above defined friction factor f can be expressed in terms of the nondimensional quantities D_h, Q and C as

$$f = \frac{D_h}{2} \frac{1}{(Q/C)^2}. \tag{25}$$

Table 1 outlines the two geometries considered in

Table 1. Different cases calculated

Case	L/b	S/L	C/L	Flow
A	11.38	1.0	0.11	Steady/unsteady
B	8.55	1.25	0.20	Steady/unsteady
C	8.55	1.25	0.20	Steady

Table 2. Summary of calculations performed for Case A (grid size 128 x 32)

Re_τ	Re_b	Re	j	f
15	35	165	0.1076	0.2919
20	58	275	0.0664	0.1873
25	84	397	0.0482	0.1406
30	112	531	0.0379	0.1131
40	171	811	0.0283	0.0862
50	285	1086	0.0244	0.0750
60	338	1347	0.0226	0.0702
80	393	1859	0.0211	0.0655
100	507	2397	0.0195	0.0616
100†	519	2455	0.0188	0.0587
100††	518	2449	0.0161	0.0590
140	735	3474	0.0179	0.0575
140‡	748	3535	0.0143	0.0555

†Two-dimensional simulation, grid size 256 x 64; ††three-dimensional simulation, grid size 256 x 64 x 64; ‡three-dimensional simulation, grid size 128 x 32 x 64.

Table 3. Summary of calculations performed for Case B (grid size 128 x 32)

Re_τ	Re_b	Re	j	f
10	18	120	0.1655	0.4427
15	37	245	0.0843	0.2385
20	57	381	0.0577	0.1747
25	82	546	0.0436	0.1330
30	105	706	0.0363	0.1147
32.5	119	797	0.0332	0.1056
35	134	899	0.0305	0.0962
40	168	1128	0.0267	0.0799
50	210	1407	0.0260	0.0802
60	249	1669	0.0250	0.0820
70	287	1923	0.0242	0.0841
70†	301	2018	0.0229	0.0764
70††	303	2029	0.0224	0.0755
80	328	2191	0.0233	0.0846

†Grid size 256 x 64; ††grid size 512 x 128.

the current study. The geometrical parameters listed are shown in Fig. 1. Case A are calculated to validate our calculation procedure with the experiments of Mullisen and Loehrke [27, 28]. The geometry represented by Case B was of primary interest to this study. Case C is similar in geometry to Case B, however, these calculations were performed on half the calculation domain in the cross-stream, y-direction and symmetry boundary conditions are applied to the top and bottom boundaries. For the geometries and Reynolds numbers considered here they symmetrized solution of Case C is steady, since asymmetry, the principal source of unsteadiness, is eliminated. Therefore Case C would correspond to the steady state calculations of Patankar and Prakash [6] and others. A comparison of results from Case B and Case C, under otherwise identical conditions, will illustrate the importance of unsteady effects. All calculations were performed by integrating the time-dependent Navier–Stokes and energy equations. We first validate our calculation procedure by doing a grid dependency study and comparing our predictions with the experiments of Mullisen and Loehrke [27, 28]. Then we point out the differences between the symmetrized steady flow (Case C) and the unsymmetrized time-dependent flow (Case B). Finally, we present the differences observed between two- and three-dimensional calculations.

2.1. *Grid dependency study*. To check the accuracy of the computer program and the resolution used in the calculations we have performed a grid dependency study for Cases A and B at high Reynolds numbers. For Case A, we increased the resolution from 128 x 32 to 256 x 64 for $Re = 2450$. We found that by doubling the resolution, the j and f factor reduced by 4% and 5%, respectively (see Table 2). Further for Case B we did a similar study at $Re = 2000$ by increasing the grid resolution from 128 x 32 to 256 x 64 and 512 x 128 (see Table 3). By doubling the grid size in each direction to 256 x 64, the f factor reduced by about 9% while the j factor reduced by 6%. Further doubling of the grid to 512 x 128 cells resulted in a nominal reduction of 1% and 2% for the f and j factors, respectively. In view of these results, we should expect deviations between +5 to +10% in the f and j factors reported on the 128 x 32 grid for $Re > 2000$ for the two-dimensional calculations.

2.2. *Effect of flow unsteadiness*. Table 2 summarizes the calculations performed for Reynolds numbers ranging from 165 to 3535 for Case A. The calculation domain was resolved with 128 x 32 finite-volume grid cells in the x- and y-directions, respectively. In the experiments of Mullisen and Loehrke [27, 28], the actual dimensions are: $L^* = 3.81$ cm, $S^* = 3.81$ cm, $C^* = 0.447$ cm and $b^* = 0.318$ cm, which yield approximately the same nondimensional ratios as shown in Table 1. The experimental results of Mullisen and Loehrke are based on the heat transfer surface area that includes only the top and bottom surfaces of the fin and ignores the front and back sides of the fin. Based on our definitions of D_h and friction factor f, we obtain the following scaling factors for D_h and f.

$$D_{h(\text{current})} = 1.846 D_{h(\text{ML})} \quad \text{and} \quad f_{(\text{current})} = 0.983 f_{(\text{ML})}. \tag{26}$$

Here no scaling is needed for the Colburn j factor. Figure 3(a)–(b) compares the current computed f and j factors with the experimental results of Mullisen and Loehrke [27, 28]. Further, we also plot the results of Sparrow and Liu [5] for an array of inline plates of infinitesimal thickness ($b = 0$), calculated for the current geometry based on their Table 1. In their calculations, Sparrow and Liu [5] assumed steady symmetric flow and solved the parabolic boundary layer equations. Because of these assumptions, their f and j factors do not include the effects of vortex shedding. In Fig. 3(a)–(b), we find that the results of Sparrow and Liu [5] agree well with the experiments and our calculations for $Re < 380$. However, there are

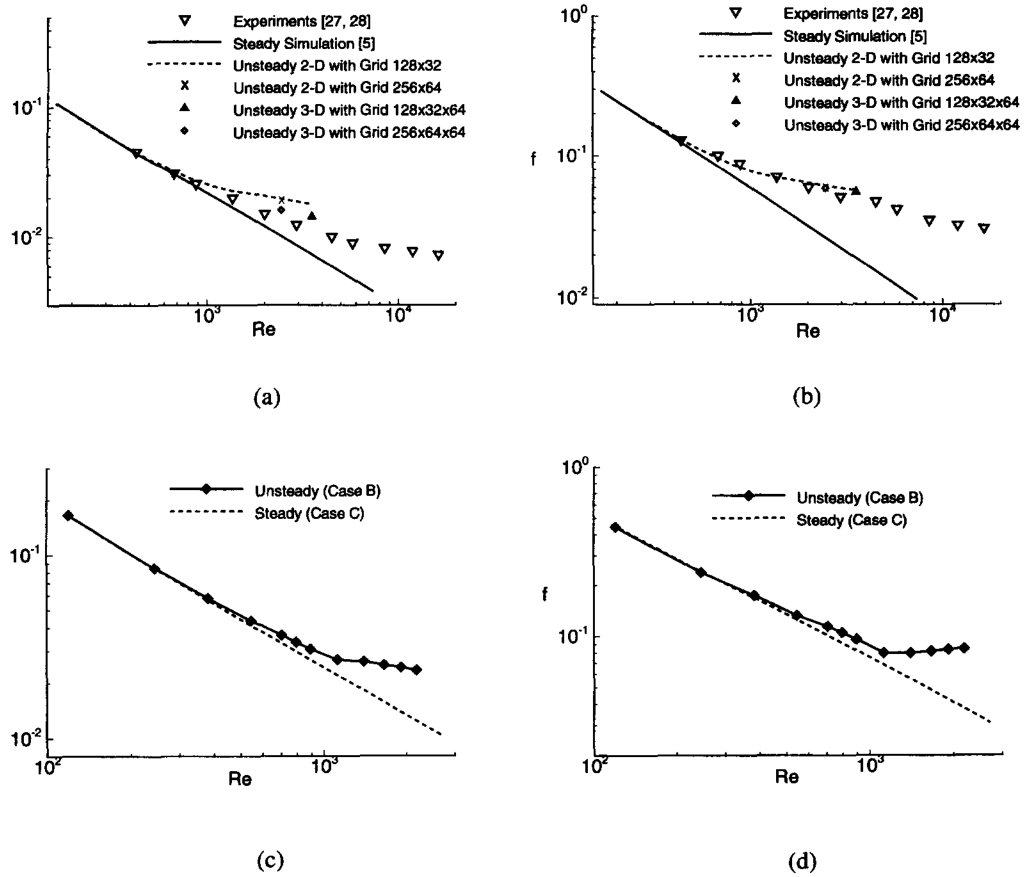

Fig. 3. Overall heat transfer and friction loss data: comparison of current results with that of existing numerical and experimental data: (a) j factor; (b) friction factor f. Comparison of unsteady simulations with steady simulations: (c) j factor; (d) friction factor f.

substantial differences for $Re > 380$, due partly to the difference in geometry (finite fin thickness vs zero fin thickness), but more importantly due to the absence of vortex shedding in their simulations. On the other hand, we find that the present time-dependent calculations show very good agreement with the experimental results upto $Re = 1300$, after which the present calculations overpredict the f and j factors. The difference in the j factor appears larger than the friction factor f.

Here it should be cautioned that while our simulations employ a constant heat flux boundary condition on fin surfaces, Mullisen and Loehrke experiments employed a constant temperature boundary condition. Furthermore Mullisen and Loehrke directly measured only the inlet and outlet fluid temperature from which j factor was iteratively by a one-dimensional energy equation for both the fin and the fluid. Additionally, while periodic boundary conditions are employed along x- and z-directions in the present computations, Mullisen and Loehrke's experiments consisted of 4 fins along the streamwise direction and 26 fins along the transverse direction. Although 4 fins along the streamwise direction may appear not to be fully sufficient for establishing a fully developed flow, there is experimental evidence that flow and thermal fields approach a fully developed state by the second fin along the streamwise direction [26]. Thus while the favorable comparison between the present simulations and the experimental results of Mullisen and Loehrke yields support for the present computational approach, the near perfect agreement at moderate Reynolds numbers maybe considered somewhat fortunate. At high Reynolds numbers, $Re > 1300$, the difference between the present simulation results and those of Mullisen and Loehrke's experiments increases. It is now well established that in bluff body wakes, by increasing the Reynolds number, three-dimensionality sets in quickly after the onset of unsteadiness [10, 11, 29]. The present two-dimensional computations ignore the effect of three-dimensionality, and thus might partially contribute to the difference. Furthermore, Mullisen and Loehrke presented evidence of paired symmetric flow and acoustic interactions which were absent in the present simulations. Here only the effect of the inclusion of intrinsic three-dimensionality will be further explored in Section 2.3.

Table 3 summarizes the calculations performed for Case B. The Reynolds number studied ranges from

Table 4. Summary of calculations performed for Case C (grid size 128 × 16)

Re_τ	Re_b	Re	j	f
10	17	117	0.1692	0.4669
15	36	240	0.0856	0.2489
20	59	392	0.0549	0.1653
25	86	573	0.0394	0.1208
30	117	784	0.0300	0.0929
30†	120	804	0.0291	0.0884
35	153	1025	0.0238	0.0740
40	194	1298	0.0194	0.0603
42†	218	1458	0.0173	0.0527
50	289	1938	0.0137	0.0423
60	405	2710	0.0103	0.0311

†Grid size 128 × 64.

approximately from 120 to 2200. Table 4 summarizes Case C, which is geometrically the same as Case B but with the calculations performed over half the computational domain with symmetric boundary conditions imposed along the transverse direction. These boundary conditions do not allow any asymmetries to develop about the centerline of the wake and hence do not allow instabilities which subsequently lead to vortex shedding. Case C corresponds to the conventional steady calculations of the time averaged Navier–Stokes and energy equations over half the calculation domain [5, 6]. A comparison of these calculations with Case B highlights the effect of unsteady vortex shedding on the f and j factors.

Figure 3(c)–(d) is plots of f and j factors calculated for Case B and Case C. The symmetrized steady flow (Case C) calculations agree well with the unsteady calculations (Case B) at low Reynolds number when the flow is steady. However, as the Reynolds number increases above 350 the differences between the two are quite clear. These differences are very evident when we compare the time-averaged mean streamline and temperature distributions. Figures 4(a)–(d) and 5(a)–(d) compare the mean streamlines and temperature profiles at Reynolds numbers of approximately 800 and 1400, respectively. At Reynolds numbers lower than 350 when the actual flow is steady, the mean streamline pattern and temperature profiles are in perfect agreement. However, as the Reynolds number increases to the unsteady regime, there are large differences in the mean flow pattern. For the symmetrized cases, the recirculation zone behind the fin increases with Reynolds number while the unsteady calculations show much smaller recirculation patterns due to the increased mixing. Correspondingly, there are large differences in the mean temperature profiles as well. These differences introduce large errors in the prediction of j and f, thus clearly illustrating the importance of accounting for flow unsteadiness at higher Reynolds numbers.

For Case B, the flow was found to be steady at $Re = 245$ with a recirculation bubble behind the trailing edge of the fin. At the next Reynolds number of $Re = 381$, periodic vortex shedding was observed to occur with a Strouhal number of 0.14, which is defined as $Str = F^*b^*/V^*$, where F^* is the dimensional primary shedding frequency. The Strouhal number remains nearly a constant upto $Re = 1128$. Okajima [30] observed similar phenomena in his experiments on the vortex-shedding frequencies of various rectangular cylinders in a uniform flow. In his experiments with a relatively high ratio of $L^*/b^* = 4$, the Strouhal number is almost independent of the Reynolds number and has a value of 0.14. Figure 6(a)–(b) shows the time history of the velocity v at $x = 0$ and $y = 0$ for flow at Reynolds number of 1407, after reaching a stationary state, and the corresponding frequency spectrum which clearly indicates a dominant nondimensional primary frequency F of 1.2 corresponding to a Strouhal number of 0.16. Figure 6(c)–(d) show the time history and corresponding frequency spectrum for the Nusselt number signal, and it is observed that the dominant frequency of 2.4 is exactly twice that of the velocity signal. Figure 7(a)–(d) shows similar plots at $Re = 2191$. At this higher Reynolds number the Strouhal number further increases to 0.17 and the frequency spectrum shows a lot more activity with the presence of low frequency oscillations in the Nusselt number signal.

Figure 8(a)–(b) shows instantaneous contours of vorticity and temperature for Case B at $Re = 1407$. Figure 8(c) shows the corresponding instantaneous local Nusselt number around the fin periphery starting from the bottom middle (marked a in Fig. 8(b)) of the fin, anti clockwise around the fin (marked b, c, d, e in Fig. 8(b)). We find that there is a strong correlation between the large scale vorticity present in the vicinity of the fin and the temperature field. The vortices act as large scale mixers and bring in cold fluid on their downstream side towards the wall. Subsequently, the fluid picks up heat from the wall and is ejected out at the upstream end of the vortex [31]. This phenomenon is clearly seen on the top and bottom surfaces of the fin, where the temperature contours are crowded near the fin surface (high thermal gradients) on the downstream side of the vortex and extend into the vortex core on the upstream side (low thermal gradients). The Nusselt number distribution on the fin surface reflects this interaction: it exhibits a peak in the down wash region (fin surface location 0.0 and 8.8) and a valley towards the upstream side of the vortex (fin surface location 12.4 and 9.4). It should be noted that although the Nusselt number reaches its highest value at the leading edge (marked d), its contribution to the global Nusselt numbers, $\langle Nu \rangle$ and $\overline{\langle Nu \rangle}$, is relative small and vortex interaction with the temperature fields at the top and bottom fin surfaces plays a more important role in determining the overall heat transfer.

2.3. *Effect of three-dimensionality.* There is mounting evidence that the onset of three-dimensionality in wakes behind bluff bodies quickly follows the onset of periodic shedding (see Williamson and Roshko [29]).

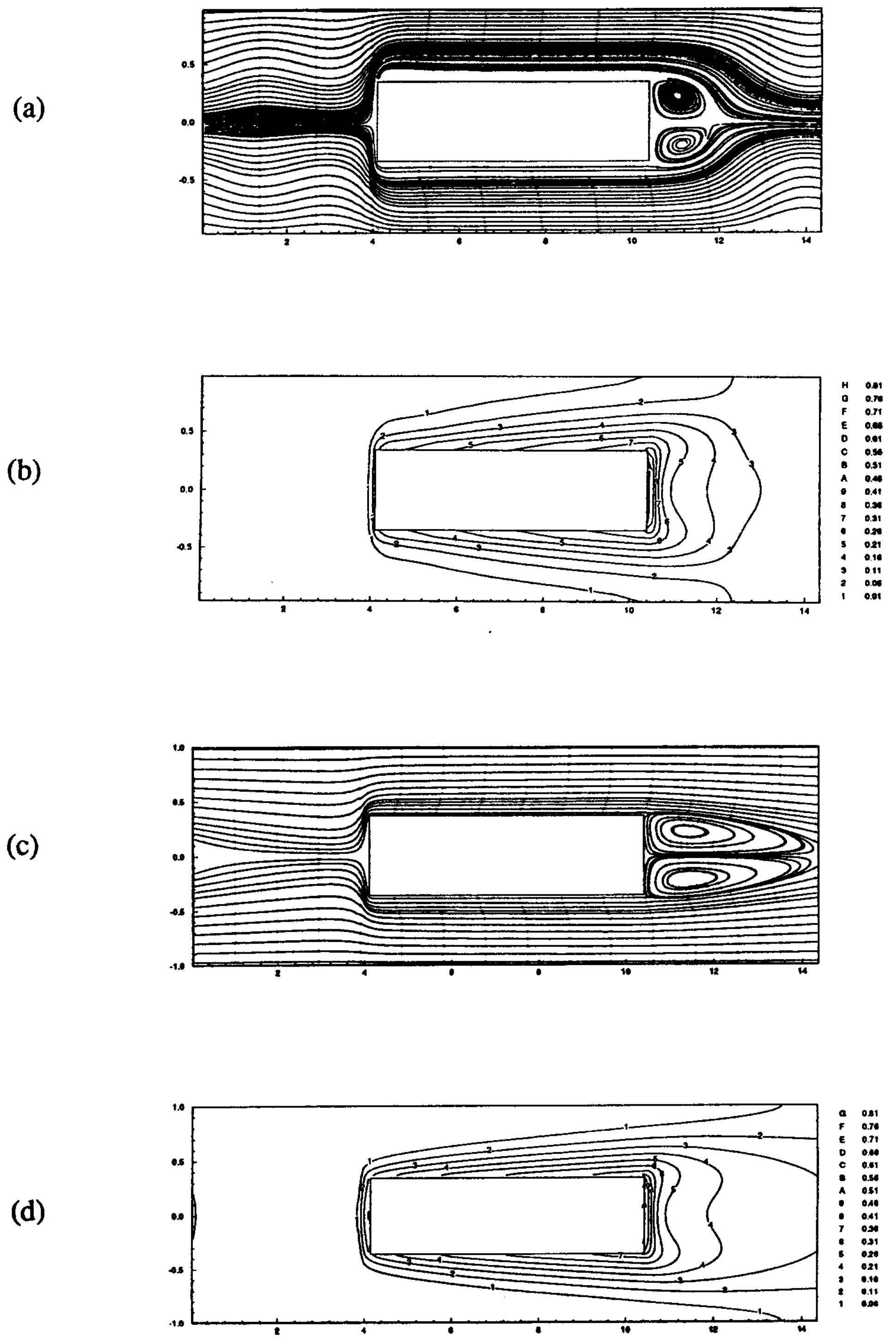

Fig. 4. (a) Streamlines and (b) temperature contours for mean flow of unsteady simulation (Case B) at $Re = 797$. (c) Streamlines and (d) temperature contours for steady symmetrized simulation (Case C) at $Re = 804$.

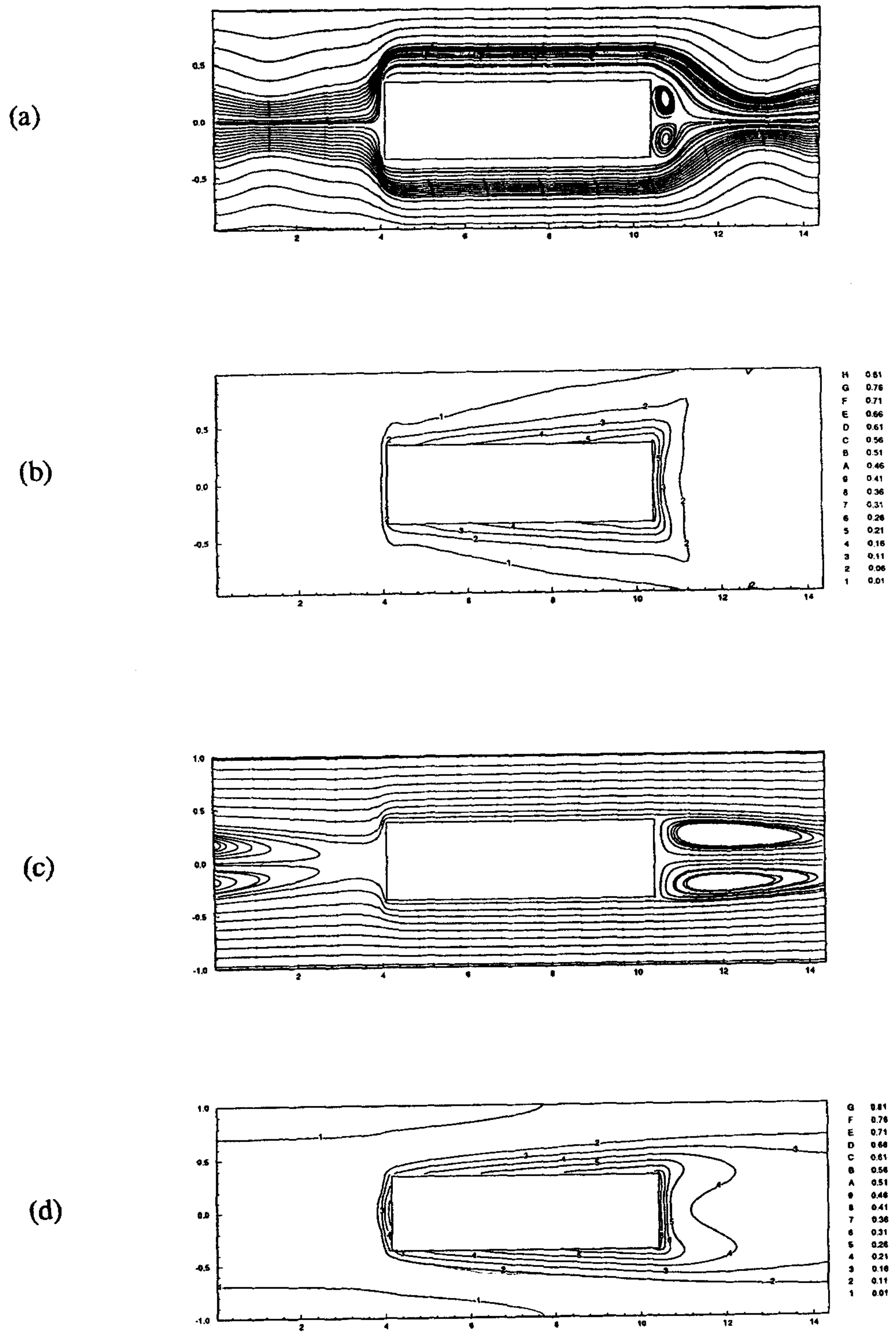

Fig. 5. (a) Streamlines and (b) temperature contours for mean flow at unsteady simulation (Case B) at $Re = 1407$. (c) Streamlines and (b) temperature contours for steady symmetrized simulation (Case C) at $Re = 1458$.

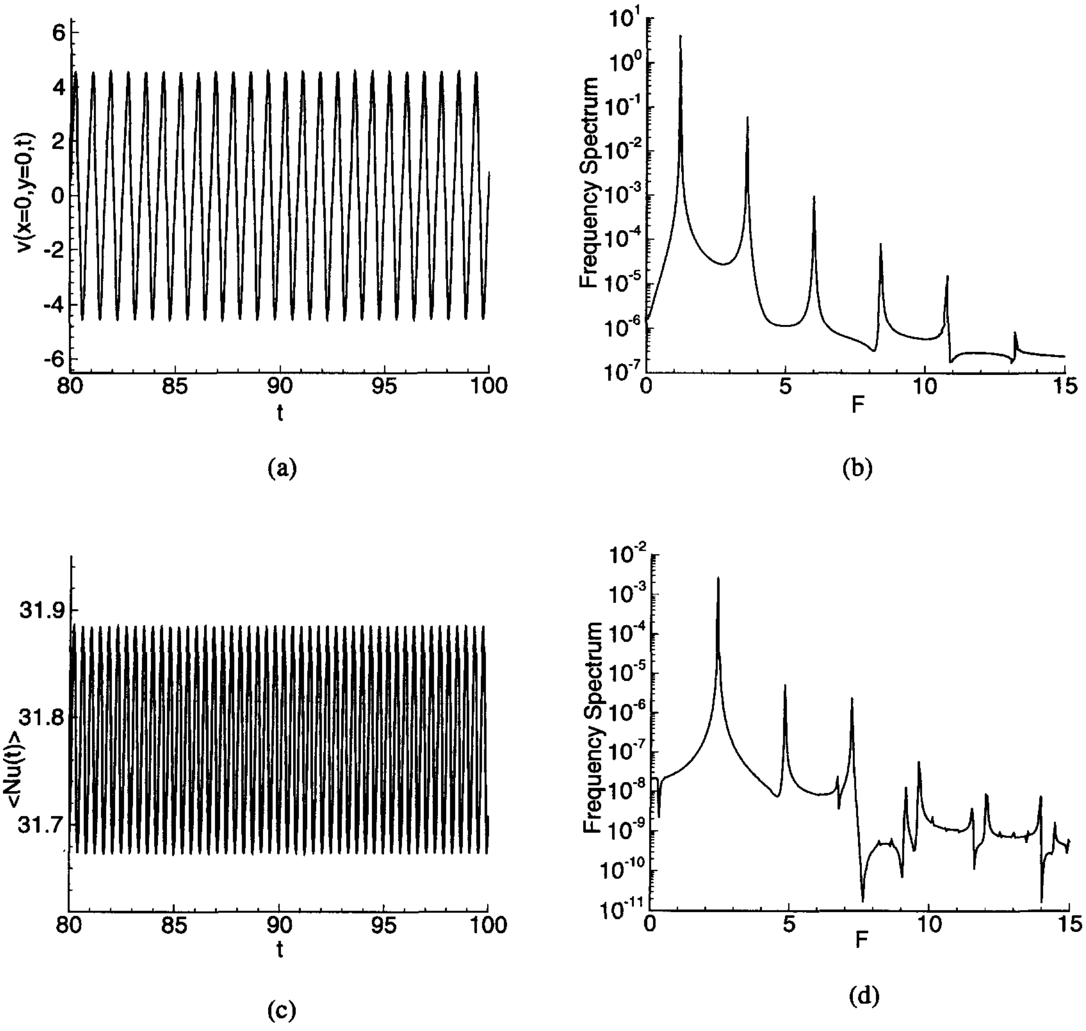

Fig. 6. Frequency analysis for flow of Case B at $Re = 1407$: (a) velocity $v(x = 0, y = 0)$ signal; (b) corresponding velocity frequency spectrum; (c) instantaneous global Nusselt number signal; (d) corresponding Nusselt number frequency spectrum.

Here we refer to intrinsic three-dimensionality resulting from fluid dynamical instabilities at sufficiently high Reynolds numbers even in the case of two-dimensional geometries, which must be separated from extrinsic three-dimensionality resulting from three-dimensional geometries. There is extensive evidence in the literature on wake flows, that 2-D models of actual 3-D flows overpredict the drag [10, 29, 32, 33]. Mittal and Balachandar [10] attribute this to higher in-plane Reynolds stresses in the wake, which substantially lowers the mean base pressure, giving a much higher form drag than in 3-D calculations. Furthermore, in two-dimensional simulations of flow over a blunt plate at $Re_b = 1000$, Tafti and Vanka [34] have found that the maximum r.m.s. value of pressure fluctuations calculated on the surface of the blunt plate is a factor of four higher than those observed in subsequent 3-D calculations (Tafti and Vanka [11]) and the experiments of Cherry *et al.* [35]. This was attributed to the strong coherence of vorticity, imposed by the two-dimensionality of the calculation. Flow visualization studies by Sasaki and Kiya [36], for uniform flow over a blunt plate, place the onset of 3-D effects soon after the separated shear layers start shedding at $Re_b = 324$. In Case A the onset of periodic shedding is observed to be around a Reynolds number of $Re = 380$ ($Re_b = 80$) and we suspect that the absence of three-dimensionality plays an important role in the increasing differences evident in Fig. 3(a–b) between our 2-D unsteady calculations and the experiments of Mullisen and Loehrke [27, 28].

To clarify this suspicion, we performed 3-D simulations for Case A at $Re = 2450$ ($Re_b = 518$) and $Re = 3500$ ($Re_b = 740$). The former calculation was performed at a resolution of $256 \times 64 \times 64$ to compare with the corresponding 2-D calculation with the resolution of 256×64, and the latter 3-D calculation used a resolution of $128 \times 32 \times 64$ to compare with the corresponding 2-D simulation of 128×32 (see Table 2). The 3-D calculations are initiated by applying a

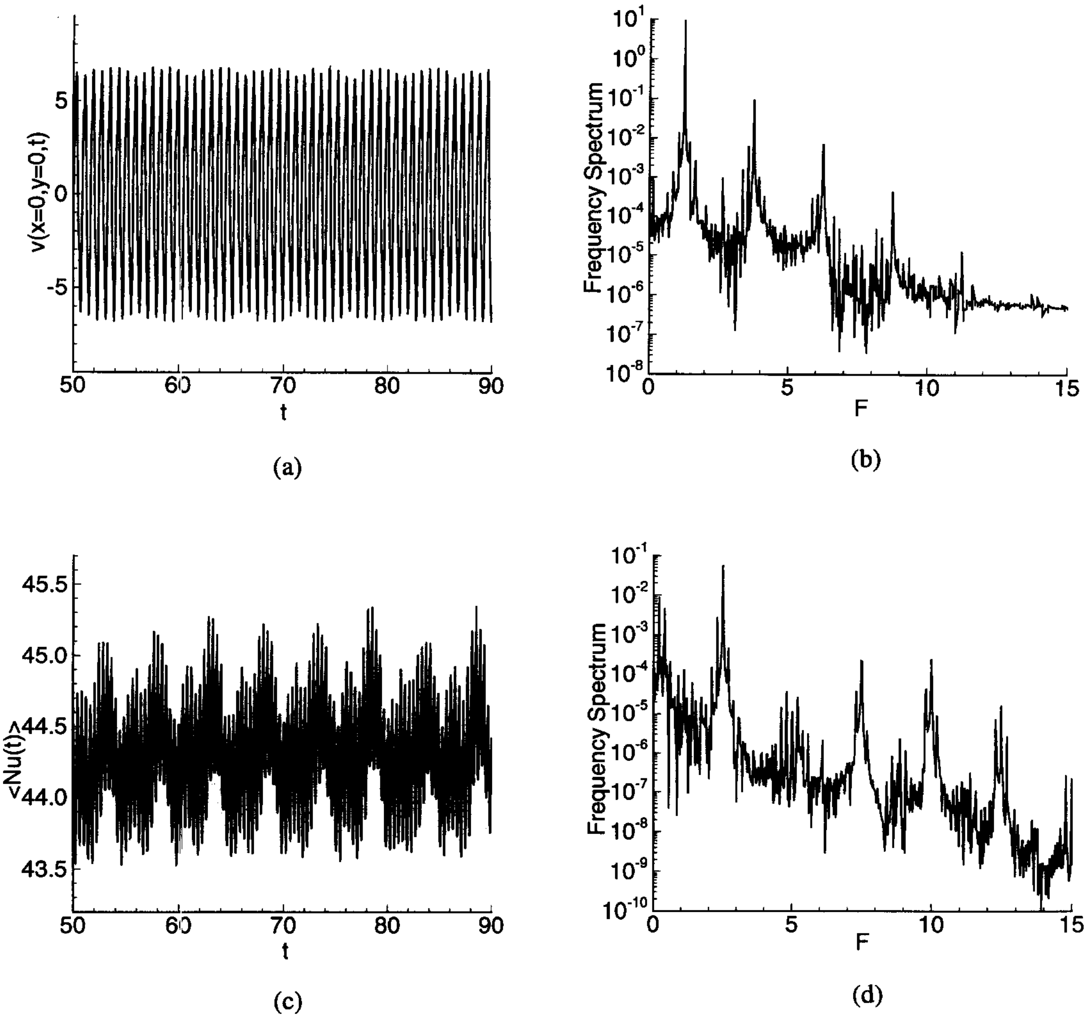

Fig. 7. Frequency analysis for flow of Case B at $Re = 2191$: (a) velocity $v(x = 0, y = 0)$ signal; (b) corresponding velocity frequency spectrum; (c) instantaneous global Nusselt number signal; (d) corresponding Nusselt number frequency spectrum.

spanwise perturbation to the corresponding 2-D flow field at one time instant. The solutions are then integrated for about 85 and 120 non-dimensional time units, respectively, well past the point when flow has become fully 3-D and reached a stationary state. The computed j and f factors from these 3-D simulations are plotted in Fig. 3(a–b), and they are in better agreement with the experimental data [27, 28]. The corresponding 2-D simulations overpredict the factor by 17% at $Re = 2450$ and by 25% at $Re = 3500$. We attribute this to the strong spanwise coherence of vorticity, which is an artifact of the two-dimensionality of the calculation. Hence, at high Reynolds number, the 2-D modeling of the 3-D flow leads to an overprediction of the j factor. Although we find that the difference in friction factor f between the two- and three-dimensional simulations at the two Reynolds numbers is within 5%, the contributions to the friction factor, from form drag and skin friction, vary considerably between the two calculations. In general, the 2-D calculation overpredicts the contribution of form drag to the overall friction factor by 15–20%. This overprediction of form drag is approximately counterbalanced by a corresponding underprediction of skin friction in the 2-D calculations, resulting in a smaller net difference in the friction factor between the two- and three-dimensional simulations.

In order to further illustrate the role of three-dimensionality, the time averaged (and also spanwise averaged in the 3-D simulation) streamlines and temperature contours for the two- and three-dimensional simulations at $Re = 2450$ are shown in Fig. 9(a–b) and (c–d), respectively. It can be seen that with the introduction of three-dimensionality, the mean wake bubble increases in size by nearly 200% and thus decreases the base suction pressure, resulting in a lower form drag in the corresponding 3-D simulation. The presence of recirculation zones near the leading edge in the 3-D simulation which is absent in the corresponding 2-D simulation also has a significant

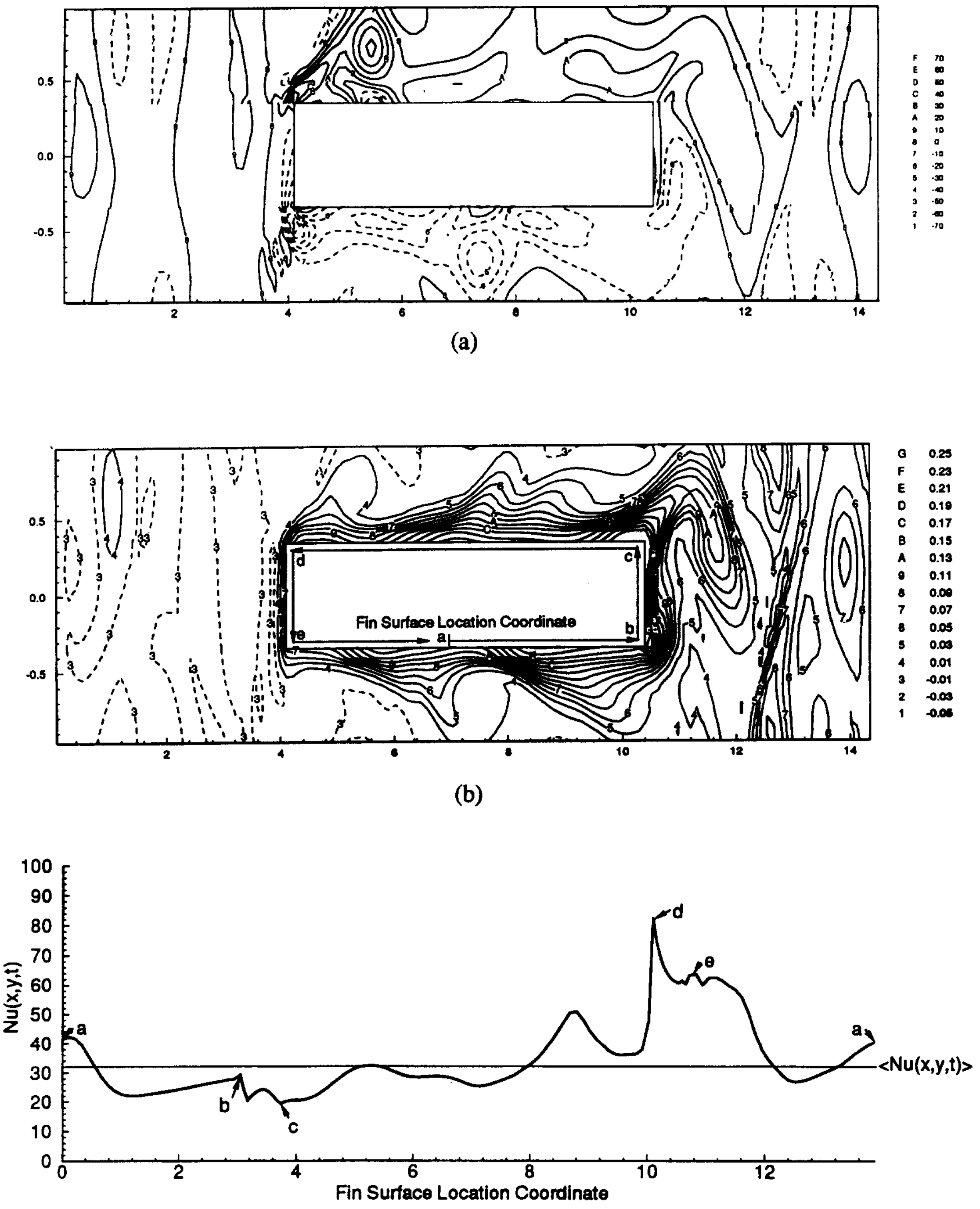

Fig. 8. Instantaneous local heat transfer enhancement of Case B at $Re = 1407$: (a) vorticity contours; (b) temperature contours; (c) local Nusselt number distribution.

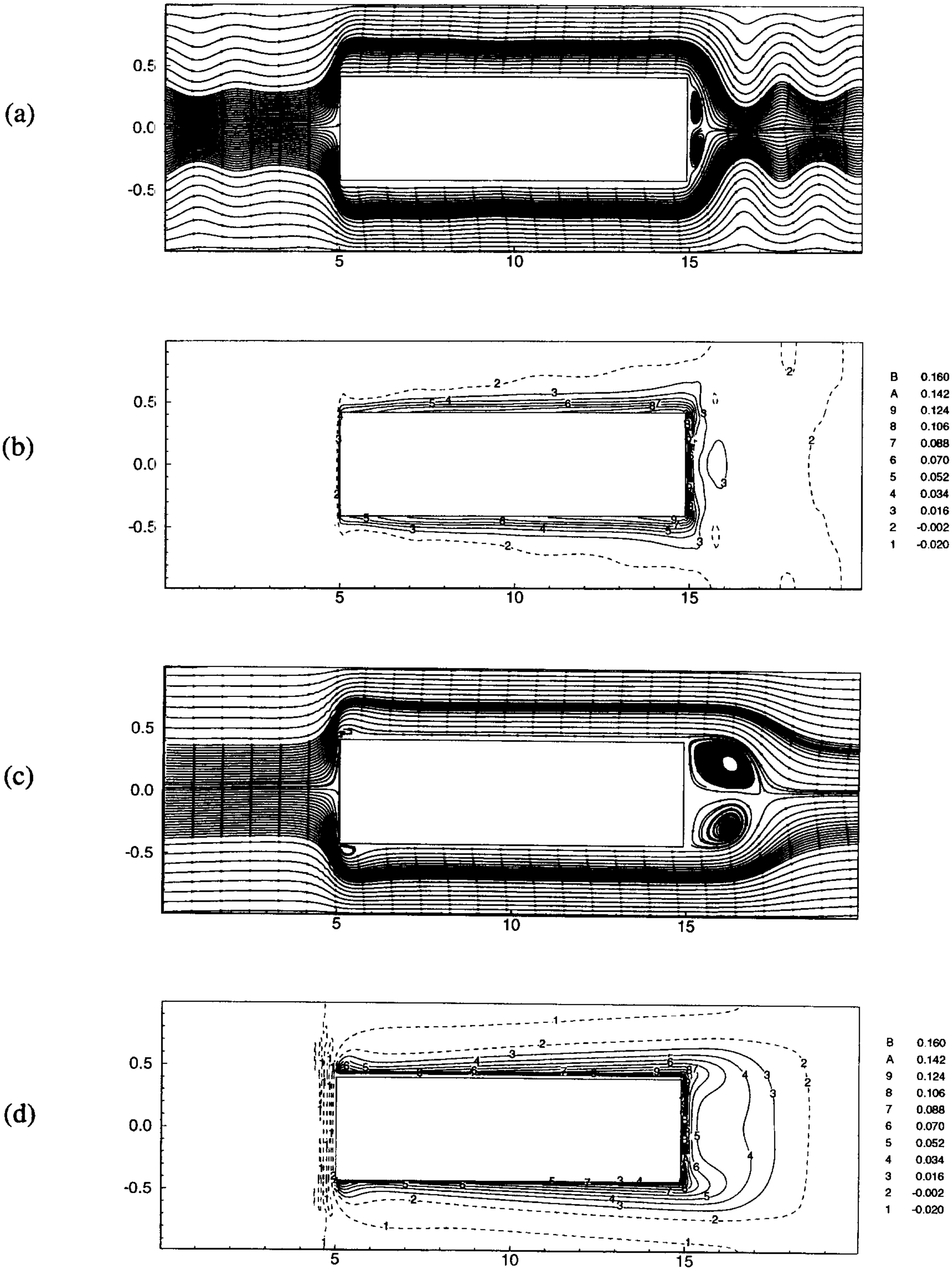

Fig. 9. Comparison of mean flows of two- and three-dimensional simulations at $Re = 2450$: (a) mean flow streamlines; (b) temperature contours from two-dimensional simulation; (c) mean flow streamlines; (d) temperature contours from three-dimensional simulation.

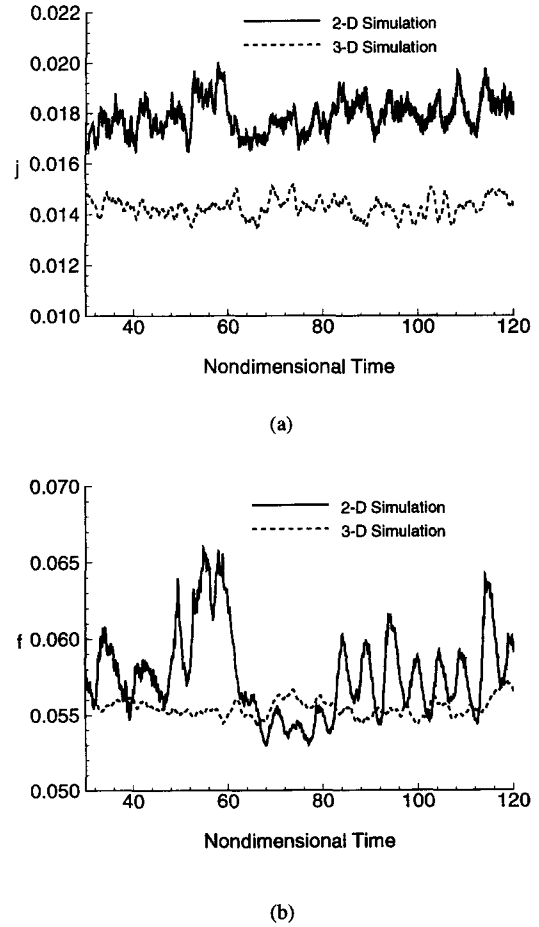

Fig. 10. Comparison of time history of overall heat transfer and friction loss quantities from two- and three-dimensional simulations at $Re = 3500$: (a) j factor; (b) friction factor f.

effect on the prediction of the overall heat transfer and skin friction, which is to reduce the heat transfer and skin friction near the leading edge. Furthermore, the fluctuations in j and f factors are much higher in the 2-D simulation than in the 3-D simulation, as shown in Fig. 10(a)–(b) for $Re = 3500$. It is observed that the amplitude of fluctuations of the friction factor f in the 2-D simulation is almost five times that in the 3-D simulation, while the amplitude of fluctuations of j factor in the 2-D simulation is almost twice that in 3-D simulation. Accurate prediction of not only the mean but also the level of fluctuation in the f and j factors becomes important in the design of heat exchangers. Therefore accounting for 3-D effects is important at higher Reynolds numbers.

CONCLUSION

In this paper we have outlined a time accurate calculation procedure for heat transfer enhancement studies in compact heat exchangers. A finite-volume based computer program is developed and implemented efficiently on the massively parallel CM-5. We have validated the performance and accuracy of the computer program for heat transfer calculations for an array of inline fins and results are in good agreement with the corresponding experimental results. A comparison of results between the conventional steady symmetrized flow calculations and the corresponding time-dependent calculations has illustrated the importance of unsteady fluctuations. It is shown that in the unsteady laminar flow regime, steady flow calculations cannot represent the enhanced large scale mixing provided by coherent vortices as they traverse the fin surface. Consequently, large errors are introduced in the predictions of the f and j factors. We also point out that intrinsic three-dimensional effects become important at high Reynolds numbers and should be taken into consideration during calculations. Although these calculations are computationally intensive, parallel architectures like the CM-5 used in the current study have made these computations possible.

Acknowledgements—The authors would like to thank the Air Conditioning and Refrigeration Center (ACRC) at the University of Illinois at Urbana-Champaign for their support. F. M. Najjar was partially supported by a NSF Division of Advanced Scientific Computing Post-doctoral Fellowship. Computation time provided on Connection Machine, CM-5, at National Center for Supercomputing Applications (NCSA) was greatly appreciated.

REFERENCES

1. Kays, W. M. and London, A. L., *Compact Heat Exchangers*. McGraw–Hill, New York.
2. Joshi, H. M. and Webb, R. L., Heat transfer and friction in the offset strip-fin heat exchangers. *International Journal of Heat and Mass Transfer*, 1987, **30**, 69–83.
3. Manglik, R. M. and Bergles, A. E., The thermal-hydraulic design of the rectangular offset-strip-fin compact heat exchanger. In *Compact Heat Exchangers*, eds R. K. Shah, A. D. Kraus and D. Metzger. Hemisphere, New York, 1990, pp. 123–149.
4. Yang, W. J., Forced convective heat transfer in interrupted compact surfaces. *Proceedings of the ASME/JSME Thermal Engineering Conference*. ASME, New York, 1983, pp. 105–111.
5. Sparrow, E. M. and Liu, C. H., Heat transfer, pressure-drop and performance relationships for inline, staggered and continuous plate heat exchangers. *International Journal of Heat and Mass Transfer*, 1979, **22**, 1613–1624.
6. Patankar, S. V. and Prakash, C., An analysis of the effect of plate thickness on laminar flow and heat transfer in interrupted-plate passages. *International Journal of Heat and Mass Transfer*, 1981, **24**, 51–58.
7. Patankar, S. V., Liu, C. H. and Sparrow, E. M., Fully developed flow and heat transfer in ducts having streamwise-periodic variations of cross-sectional area. *Journal of Heat Transfer*, 1977, **99**, 180–186.
8. Ghaddar, N. K., Karniadakis, G. E. and Patera, A. T., A conservative isoparametric spectral element method for forced convection: application to fully developed flow in periodic geometries. *Numerical Heat Transfer*, 1986, **9**, 277–300.
9. Amor, C. H. and Mikic, B. B., Spectral element simulations of unsteady forced convective heat transfer: application of compact heat exchanger geometries. *Numerical Heat Transfer, Part A*, 1991, **19**, 1–19.
10. Mittal, R. and Balachandar, S., Effect of three-dimen-

sionality on the lift and drag of circular and elliptic cylinders. *Physics of Fluids*, 1995, **7**, 1841–1865.
11. Tafti, D. K. and Vanka, S. P., A three-dimensional numerical study of flow separation and reattachment on a blunt plate. *Physics of Fluids A*, 1991, **3**, 2887–2909.
12. Gresho, P. M. and Sani, R. L., On pressure boundary conditions for the incompressible Navier–Stokes equations. *International Journal of Numerical Methods in Fluids*, 1987, **7**, 1111–1145.
13. Williams, P. T. and Baker, A. J., Incompressible computational fluid dynamics and the continuity constraint method for the three-dimensional Navier–Stokes equations. *Numerical Heat Transfer, Part B*, 1996, **29**, 137–273.
14. Harlow, F. H. and Welch, J. E., Numerical calculation of time-dependent viscous incompressible flow of fluid with free surface. *Physics of Fluids*, 1965, **8**, 2181–2189.
15. Chorin, A. J., Numerical solution of the Navier–Stokes equations. *Mathematic Computing*, 1968, **22**, 745–762.
16. Kim, J. and Moin, P., Application of a fractional-step method to incompressible Navier–Stokes equations. *Journal of Computational Physics*, 1985, **59**, 308–323.
17. Wu, J., Sheridan, J., Soria, J. and Welsh, M. C., An experimental investigation of the steamwise vortices in the wake of a bluff body. *Journal of Fluids Structures*, 1994, **8**, 621–635.
18. Mansy, H., Yang, P.-M. and Williams, D. R., Quantitative measurements of three-dimensional structures in the wake of a circular cylinder. *Journal of Fluid Mechanics*, 1994, **270**, 277–296.
19. Henderson, R. D., Unstructured spectral element methods: Parallel algorithms and simulations. Ph.D. thesis, Princeton University, Princeton, NJ, 1994.
20. Williamson, C. H. K., The existence of two stages in the transition to three-dimensionality of a cylinder wake. *Physics of Fluids*, 1988, **31**, 3165–3168.
21. Tafti, D. K., High-order finite difference formulation for the incompressible Navier–Stokes equations on the CM-5. *Proceedings of the Seventh SIAM Conference on Parallel Processing for Scientific Computing*, 1995, 155–160.
22. Tafti, D., Comparison of some upwind biased high-order formulations with a second-order central difference scheme for time integration of the incompressible Navier–Stokes equations. *Computers and Fluids*, 1996, **25**, 647–665.
23. Tafti, D. K., Features and implementation issues for a high-order finite difference algorithm for direct and large eddy simulations of incompressible turbulence on the CM-5. NCSA technical report 047, NCSA, 1994.
24. Hestenes, M. and Stiefel, E., Methods of conjugate gradients for solving linear systems. *Journal of Research Bureau Standards*, 1952, **49**, 409–436.
25. Tafti, D. K., A study of Krylov methods for the solution of the pressure poisson equation on the CM-5. In *Numerical Developments in CFD*, ed. M. N. Dhaubhadel *et al.*, FED-VOl. 215, ASME, New York, 1995, pp. 1–8.
26. Sparrow, E. M. and Hajiloo, A., Measurements of heat transfer and pressure drop for an array of staggered plates aligned parallel to an air flow. *J. Heat Transfer*, 1980, **102**, 426–432.
27. Mullisen, R. S. and Loehrke, R. I., A study of the flow mechanisms responsible for heat transfer enhancement in interrupted-plate heat exchangers. *Journal of Heat Transfer*, 1986, **108**, 377–385.
28. Mullisen, R. S., Heat transfer, pressure drop, and fluid flow in interrupted wall passages. Ph.D. thesis, Colorado State University, Fort Collins, CO, 1983.
29. Williamson, C. H. K. and Roshko, A., Measurements of base pressure in the wake of a cylinder at low Reynolds numbers. *Zeitschrift Flugwissenschaft Weltraumforch*, 1990, **14**, 38–46.
30. Okajima, A., Strouhal numbers of rectangular cylinders. *Journal of Fluid Mechanics*, 1982, **123**, 379–398.
31. Tafti, D. K., Vorticity dynamics and scalar transport in separated and reattached flow on a blunt plate. *Physics of Fluids A*, 1991, **5**, 1661–1673.
32. Tamura, T., Numerical study of aerodynamic behavior of square cylinders. *Journal of Wind Engineering and Industrial Aerodynamics*, 1990, **33**, 161–170.
33. Tamura, T., On the reliability of two-dimensional simulation for unsteady flows around a cylinder-type structure. *Journal of Wind Engineering and Industrial Aerodynamics*, 1990, **35**, 275–298.
34. Tafti, D. K. and Vanka, S. P., A numerical study of flow separation and reattachment on a blunt plate. *Physics of Fluids A*, 1991, **3**, 1749–1759.
35. Cherry, N. J., Hillier, R. and Latour, M. P., Unsteady measurements in a separated and reattaching flow. *Journal of Fluid Mechanics*, 1984, **144**, 13–46.
36. Sasaki, K. and Kiya, M., Three-dimensional vortex structure in a leading-edge separation bubble at moderate Reynolds numbers. *Journal of Fluids Engineering*, 1991, **113**, 405–410.